Model for atomic dielectric response in strong, time-dependent laser fields

T. C. Rensink, T. M. Antonsen, Jr., and J. P. Palastro
University of Maryland, College Park, Maryland 20742, USA

D. F. Gordon
Naval Research Laboratory, Plasma Physics Division, Washington DC, 20375, USA

(Received 12 December 2013; published 14 March 2014)

A nonlocal quantum-mechanical model is presented for calculating the atomic dielectric response to a strong laser electric field. By replacing the Coulomb potential with a nonlocal potential in the Schrödinger equation, a $3+1$-dimensional calculation of the time-dependent electric dipole moment can be reformulated as a $0+1$-dimensional integral equation that retains the three-dimensional dynamics, while offering significant computational savings. The model is benchmarked against an established ionization model and *ab initio* simulation of the time-dependent Schrödinger equation. The reduced computational overhead makes the model a promising candidate to incorporate full quantum-mechanical time dynamics in laser pulse propagation simulations.

DOI: 10.1103/PhysRevA.89.033418 PACS number(s): 32.80.Rm, 32.80.Wr, 31.15.−p

I. INTRODUCTION

High intensity ultrashort laser propagation gives rise to a wide range of phenomena and has been an integral part of several fields of research over the past few decades, such as laser-wake-field acceleration [1], generation of terahertz radiation [2,3], high harmonic generation [4], and atmospheric filamentation [5–8]. For laser intensities near the ionization threshold of tenuous propagation media, field and medium dynamics are strongly nonlinear in the electric field, requiring numerical simulation for proper treatment. In principle, this could be accomplished by calculating the self-consistent evolution of all fields and charges in the system. Consider for a moment a collection of noninteracting hydrogen atoms: for each atom with center of mass at position $\mathbf{R}$, we can express the atomic dipole moment in terms of the relative coordinate, $\mathbf{r}' \equiv \mathbf{r} - \mathbf{R}$:

$$\mathbf{d}(\mathbf{R},t) \equiv -e\langle \mathbf{r}'(t)\rangle, \tag{1}$$

where $\langle \mathbf{r}'(t)\rangle \equiv \int d^3\mathbf{r}'\ \psi^*(\mathbf{r}',t)\mathbf{r}'\psi(\mathbf{r}',t)$ is the expectation value of the electron position relative to $\mathbf{R}$ in terms of the electron wave function, $\psi(\mathbf{r}',t)$. The dielectric contribution over all of the atoms can be smoothed over some region and weighted by the local gas density $n_g(\mathbf{R})$ to give the macroscopic polarization density

$$\mathbf{P}(\mathbf{R},t) = n_g(\mathbf{R})\mathbf{d}(\mathbf{R},t) \tag{2}$$

that appears as a source term in a propagation equation for the laser electric field $\mathbf{E}(\mathbf{R},t)$; iteratively solving $\mathbf{P}(\mathbf{R},t)$ and $\mathbf{E}(\mathbf{R},t)$ allows one to solve for future states of the system. In practice, simulating laser pulse propagation over macroscopic distances is complicated by the need to include quantum-mechanical laser-atom dynamics at atomic scales. While calculations of this kind have been performed for single atoms with the time-dependent Schrödinger equation (TDSE), such simulations generally require supercomputing resources, and scaling this up to a full three-dimensional (3D) laser propagation simulation is a task well beyond current capabilities.

Instead, the "standard" treatment [5,9–11] of material dielectric response in propagation simulations consists of breaking the total polarization density in Eq. (2) into separate terms. In the limit that the laser field is small compared with the atomic field, a "bound" atomic response is given by a perturbative expansion in the laser field strength, and terms are included that are proportional to powers of the laser electric-field strength, such as $\mathbf{P}^{(1)} \propto \mathbf{E}$ and $\mathbf{P}^{(3)} \propto \mathbf{E}^3$. For larger field strengths, electron ionization becomes important, giving rise to "free" electrons that contribute a plasma response. Laser induced ionization is a rich subject in itself and has given rise to many theoretical [12–17] and experimental [18,19] studies over the years. While such models are based on various approximations and do not include the time history of the material response, they are nevertheless employed for efficiency to calculate terms for plasma response and field energy lost due to ionization.

The shortcomings of this treatment are reflected in the fact that several terms are necessary to describe the total nonlinear polarization density given in Eq. (2). While *ab initio* quantum simulations are not possible for the reason stated above, we explore a nonlocal interaction (NLI) model [20] that offers a promising alternative: by replacing the Coulomb potential with a nonlocal potential term in the 3D TDSE, a computationally inexpensive method can be used to calculate $\mathbf{d}(\mathbf{R},t)$ for a single atom, putting a nonfragmented treatment of $\mathbf{P}(\mathbf{R},t)$ for laser propagation simulations within reach. Our objectives for this paper are then twofold: present the NLI model, and motivate its validity. Sections II and III introduce the formulation of the NLI model and explain the method used for fast computation. Section IV gives expressions for the ionization rate, bound-electron probability, and expectation value of the electron position that are used to benchmark the NLI model in Sec. V. Finally, Sec. VI briefly outlines an extension to include an arbitrary number of bound states. Other detailed analyses are deferred to the Appendix to permit continuity of the main text.

II. NLI MODEL FORMULATION

We consider a single atom of hydrogen at the origin, such that $\mathbf{R} = 0$ and $\mathbf{r}' = \mathbf{r}$ (the convention used hereafter). The 3D TDSE for a single electron under the influence of a Coulomb

potential and subject to a time varying electric field $\mathbf{E}(t)$ in the dipole approximation is

$$i\hbar\frac{\partial}{\partial t}\psi(\mathbf{r},t) = \left[-\frac{\hbar^2}{2m_e}\nabla^2 - \frac{Ze^2}{|\mathbf{r}|} + e\mathbf{E}(t)\cdot\mathbf{r}\right]\psi(\mathbf{r},t). \quad (3)$$

The nonlocal interaction potential (NLI) model is formulated by replacing the Coulomb potential in Eq. (3) with a nonlocal potential term

$$-\frac{Ze^2}{|\mathbf{r}|}\psi(\mathbf{r},t) \to -Vu(\mathbf{r})S(t),$$

where

$$u(\mathbf{r}) \equiv (\pi\sigma^2)^{-3/4}\exp(-\mathbf{r}^2/2\sigma^2), \quad (4a)$$

$$S(t) \equiv \int d^3\mathbf{r}\, u(\mathbf{r})\psi(\mathbf{r},t). \quad (4b)$$

Here $u(\mathbf{r})$ represents the spatial extent of the binding potential, while $S(t)$ is the "nonlocal" portion of the potential. Using the shorthand notation $\langle f(\mathbf{r})|g(\mathbf{r})\rangle \equiv \int d^3\mathbf{r}\, f(\mathbf{r})g(\mathbf{r})$, it can be seen from Eq. (4a) that $u(\mathbf{r})$ is a normalized function such that $|\langle u|u\rangle|^2 = 1$ and $S(t) = \langle u(\mathbf{r})|\psi(\mathbf{r},t)\rangle$ is the projection of the time-dependent wave function onto $u(\mathbf{r})$. We have introduced two free parameters with the above definitions: V, the normalized binding energy, used to change the overall strength of the binding potential, and σ, the spatial extent of the binding potential. These may be chosen to match the ionization properties of atomic hydrogen, as will be seen later.

It is not immediately apparent that this is an appropriate replacement for the Coulomb potential, and a few comments are in order to motivate this substitution. In the limit $\sigma \to 0$, $u(\mathbf{r})$ becomes a δ function and the NLI potential recovers the familiar local potential term, $-\lambda\delta^3(\mathbf{r})\psi(\mathbf{r},t)$; while the δ potential has been considered in 1D treatments of Eq. (3) [21], the 3D extension produces solutions to $\psi(\mathbf{r})$ that are singular at the origin. The NLI potential can be considered one modification of the 3D δ function that permits normalizable solutions to the wave function. The NLI model has the desirable features that it is Hermitian, norm-preserving, and linear in $\psi(\mathbf{r},t)$. However, it is not gauge invariant, and we have written the Hamiltonian in the form in which the time-dependent field enters as a potential. The consequences of the nongauge invariance remain to be explored. For simplicity, all equations and mathematical expressions in the remainder of this paper will use the following normalization convention unless otherwise specified: $\mathbf{r}/\sigma \to \mathbf{r}$, $\hbar t/m_e\sigma^2 \to t$, $m_e\sigma^2 V/\hbar^2 \to V$, and $\sigma^3 m_e e\mathbf{E}(t)/\hbar^2 \to \mathbf{E}(t)$. These are identical to atomic units except that all factors of length are scaled to $\sigma \equiv \beta a_0$ (β const) instead of the Bohr radius. Although this normalization choice hides all factors of the free parameter σ, for which we have not yet specified the value, it has the advantage of producing considerably simpler algebraic expressions than atomic units would produce. Below are the previously defined quantities in the normalized coordinates, as well as the modified TDSE. Together, these define the complete system we wish to solve for a general electric field $\mathbf{E}(t)$:

$$u(\mathbf{r}) = \pi^{-3/4}\exp(-\mathbf{r}^2/2), \quad (5a)$$

$$S(t) = \int d^3\mathbf{r}\, u(\mathbf{r})\psi(\mathbf{r},t), \quad (5b)$$

$$i\frac{\partial}{\partial t}\psi(\mathbf{r},t) = \left[-\frac{1}{2}\nabla^2 + \mathbf{r}\cdot\mathbf{E}(t)\right]\psi(\mathbf{r},t) - Vu(\mathbf{r})S(t). \quad (5c)$$

III. REDUCTION TO 1D INTEGRAL EQUATION

In principle, the system given by Eqs. (5) could be simulated directly by time evolving the modified Schrödinger equation with a finite-difference [22], finite-volume [23], or spectral method [24], and quantities of interest could be obtained through the usual prescription of operators and expectation values. This would be a computational task essentially equal to solving the original TDSE, with no advantage gained by using the modified binding potential. However, the NLI model offers a considerably different approach to obtain the same information. Specifically, we reduce the system given by Eqs. (5) to an integral equation in time for $S(t)$ without explicitly calculating $\psi(\mathbf{r},t)$. Quantities of interest, such as the dipole moment $\mathbf{d}(t)$ and the bound probability of the electron can, in turn, be derived directly in terms of $S(t)$, thereby eliminating the need to solve for the wave function altogether.

The computational savings of the NLI model are a direct result of the fact that no spatial representation for $\psi(\mathbf{r},t)$ is required to be calculated to obtain information about the system. By contrast, a typical finite volume treatment of the TDSE calculates $\psi(\mathbf{r},t)$ on a spatial grid and evolves it at each point in space over time. Accurate calculation of $\langle\mathbf{r}(t)\rangle$ requires the spatial domain to be large enough to capture free-wave-function excursions on the order of the quiver radius $r_q = e|E_L|/m_e\omega_L^2$ (where ω_L and E_L are the frequency and amplitude of the applied field respectively) while maintaining sufficient spatial resolution to resolve the wave function of large momentum states. The time domain must resolve the period of the quantum bound state (typically subfemtosecond), while extending over the duration of the laser pulse simulation, often on the order of hundreds of femtoseconds. While still subject to the same time domain constraints, the NLI approach lifts the restrictions in the spatial domain entirely, as will be seen.

A Green's-function (or propagator) approach will be used to obtain the integral equation for $S(t)$. We first define $G(\mathbf{r},t;t')$ as the solution to the equation

$$\left[i\frac{\partial}{\partial t} + \frac{1}{2}\nabla^2 - \mathbf{r}\cdot\mathbf{E}(t)\right]G(\mathbf{r},t;t') = iu(\mathbf{r})\delta(t-t'), \quad (6)$$

where we have taken Eq. (5c) and replaced $-VS(t)$ by an impulse in the time domain, $i\delta(t-t')$, and the boundary condition is taken to be $G(\mathbf{r},t<t';t') = 0$. Because the electric potential term $-\mathbf{r}\cdot\mathbf{E}(t)$ is linear in space, Eq. (6)

admits a closed-form solution,

$$G(\mathbf{r},t;t') = \frac{1}{\pi^{3/4}\,[1+i(t-t')]^{3/2}} \times \exp\left[i\mathscr{S}_0 + i\mathbf{v}_0\cdot(\mathbf{r}-\mathbf{r}_0) - \frac{|\mathbf{r}-\mathbf{r}_0|^2}{2+2i(t-t')}\right]. \tag{7}$$

The function $G(\mathbf{r},t;t')$ depends on the trajectories of a classical electron, designated with subscript "0," subject to field $\mathbf{E}(t)$. Here, $\mathbf{r}_0(t;t')$, $\mathbf{v}_0(t;t')$, and $\mathscr{S}_0(t;t')$, represent the position, velocity, and action of a classical electron, related through the coupled ordinary differential equations with associated initial conditions:

$$\frac{d\mathbf{r}_0}{dt} = \mathbf{v}_0(t), \tag{8a}$$

$$\frac{d\mathbf{v}_0}{dt} = -\mathbf{E}(t), \tag{8b}$$

$$\mathscr{S}_0(t,t') \equiv \int_{t'}^{t} dt''\left[\frac{1}{2}\mathbf{v}_0^2(t'') - \mathbf{r}_0(t'')\cdot\mathbf{E}(t'')\right], \tag{8c}$$

where

$$\mathbf{v}_0(t=t';t') = \mathbf{r}_0(t=t';t') = 0. \tag{8d}$$

Conceptually, these trajectories describe the path of an electron "born" at the origin with zero initial velocity at t' and subsequently moving under the force of the electric field until t. With the function $G(\mathbf{r},t;t')$ defined by Eqs. (6) and (7) we can express the wave function as a convolution,

$$\psi(\mathbf{r},t) = iV\int_{-\infty}^{t} dt' G(\mathbf{r},t;t')S(t'). \tag{9}$$

To make use of this expression for $\psi(\mathbf{r},t)$, $S(t')$ must be known on the interval $-\infty < t' \leqslant t$. For problems of interest, we will assume that the wave function is in the bound state and $\mathbf{E}(t) = 0$ for $t \leqslant 0$: this constraint is sufficient to obtain an analytic expression for $S(t' < 0)$, as shown in the next section. For $t > 0$ (after the field is present) values of $S(t')$ are calculated with a general expression, obtained in the following way: on inserting Eq. (9) into Eq. (5b) and integrating over all space, an integral equation in time for $S(t)$ for general field $\mathbf{E}(t)$ is given by

$$S(t) = i2^{3/2}V\int_{-\infty}^{t} dt' S(t')\frac{\exp[i\mathscr{S}_0(t,t') + \Lambda(t,t')]}{[2+i(t-t')]^{3/2}}, \tag{10}$$

where

$$\Lambda(t,t') \equiv \frac{1+i(t-t')}{2+i(t-t')}\frac{|\mathbf{r}_0 - i\mathbf{v}_0|^2}{2} - \frac{1}{2}|\mathbf{r}_0|^2.$$

Equation (10) will be used to calculate the time dependence of all quantities of interest, including the dipole moment and $\psi(\mathbf{r},t)$ via Eq. (9), and as such is the primary computational task in the NLI model. The time savings over typical TDSE treatments is manifest by the absence of any spatial dependence in Eq. (10). One might protest that we have traded the problem of a large spatial simulation domain for an infinite time integral, but solving for $S(t)$ via Eq. (10) is more tractable than it might seem: as with Eq. (9), the explicit form of $S(t')$ on $-\infty < t' \leqslant 0$ is obtained with the condition that the electron is bound on this interval, while subsequent values of $S(t)$ can be calculated numerically via Eq. (10). A more detailed discussion of the numerical treatment of Eq. (10) is given in the Appendix.

IV. PROPERTIES OF THE NLI MODEL

A. Field-free system

To better understand the nonlocal potential, we first examine the system in the absence of an applied field. For $\mathbf{E}(t) = 0$, the NLI potential admits a single bound state $\psi_0(\mathbf{r})$ with energy E_0 that can be determined as follows: With no applied field, classical variables $\mathbf{r}_0(t,t')$, $\mathbf{v}_0(t,t')$, and $\mathscr{S}_0(t,t')$ in Eqs. (8) are identically zero, and Eq. (10) simplifies to a convolution whose kernel depends only on the time difference $(t-t')$,

$$S(t) = i2^{3/2}V\int_{-\infty}^{t} dt' \frac{S(t')}{[2+i(t-t')]^{3/2}}. \tag{11}$$

Solutions of Eq. (11) are of the form $S(t) = S_0 e^{-iE_0 t}$, where S_0 is a complex constant. Inserting this expression into Eq. (11) results in a transcendental equation for the energy E_0 given by

$$V = \frac{1}{4}[1 - \sqrt{2\pi|E_0|}e^{2|E_0|}\mathrm{erfc}(\sqrt{2|E_0|})]^{-1}. \tag{12}$$

The expression in Eq. (12) is plotted in Fig. 1(a). Sufficiently large values of V correspond to a single bound-state wave function of the form $\psi(\mathbf{r},t) = \psi_0(\mathbf{r})e^{-iE_0 t}$ and eigenvalue E_0. An expression for the bound-state wave function can be found by inserting Eq. (7) into Eq. (9) with $\mathbf{r}_0, \mathbf{v}_0, \mathscr{S}_0 = 0$, and $S(t) = S_0 e^{-iE_0 t}$ to give

$$\psi_0(\mathbf{r}) = i\frac{S_0 V}{\pi^{3/4}}\int_0^{\infty} dt' \frac{e^{iE_0 t'}}{[1+it']^{3/2}}\exp\left[\frac{-|\mathbf{r}|^2}{2+2it'}\right]. \tag{13}$$

The profile of $\psi_0(\mathbf{r})$ is plotted in Fig. 1(b) alongside $u(\mathbf{r})$ for comparison.

B. Dipole moment

With the ultimate goal of finding the polarization density in mind, we seek a computationally efficient expression for the atomic dipole $\mathbf{d}(t) = -\langle\mathbf{r}(t)\rangle$ expressed in terms of $S(t)$ without explicit reference to $\psi(\mathbf{r},t)$. We start with the definitions of the expectation values for normalized position and momentum,

$$\langle\mathbf{r}(t)\rangle \equiv \int d^3\mathbf{r}\;\psi^*(\mathbf{r},t)\,\mathbf{r}\,\psi(\mathbf{r},t), \tag{14}$$

and

$$\langle\mathbf{p}(t)\rangle \equiv -i\int d^3\mathbf{r}\;\psi^*(\mathbf{r},t)\nabla\psi(\mathbf{r},t), \tag{15}$$

noting that both $\langle\mathbf{r}(t)\rangle$ and $\langle\mathbf{p}(t)\rangle$ are real. A set of ordinary differential equations relating $\langle\mathbf{r}(t)\rangle$ and $\langle\mathbf{p}(t)\rangle$ is obtained by following the steps used to derive the Ehrenfest relations. The result is similar to Eqs. (8) with additional terms resulting from the nonlocal binding potential:

$$\frac{d\langle\mathbf{r}(t)\rangle}{dt} = \langle\mathbf{p}(\mathbf{t})\rangle - 2V\;\mathrm{Im}\{S(t)\nabla_0 S^*(t)\}, \tag{16a}$$

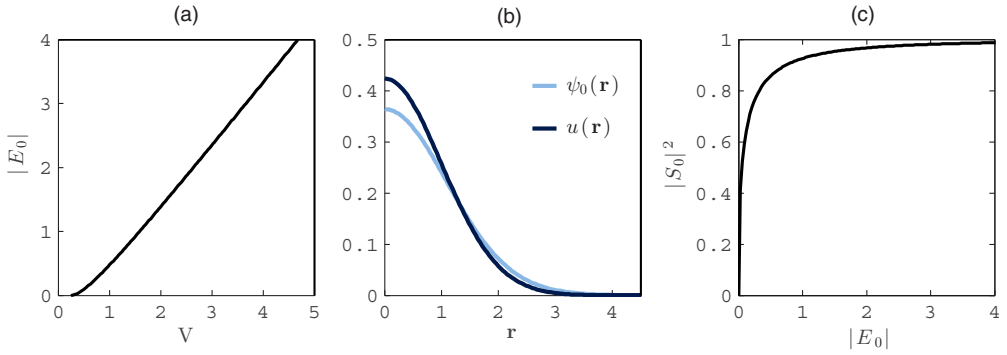

FIG. 1. (Color online) (a) Normalized bound-state energy E_0 as a function of normalized potential strength V. Sufficiently small V does not admit a bound state. (b) Normalized profiles for the bound-state wave function $\psi_0(\mathbf{r})$ and the NLI function $u(\mathbf{r})$ for parameter values $V = 3.77$, $\sigma = 2.494a_0$ used for modeling atomic hydrogen. (c) The quantity $|S_0|^2 = |\langle u(\mathbf{r})|\psi_0(\mathbf{r})\rangle|^2$ as a function of normalized bound-state energy: $\psi_0(\mathbf{r})$ approaches $u(\mathbf{r})$ in the high-energy limit.

and

$$\frac{d\langle \mathbf{p}(\mathbf{t})\rangle}{dt} = -\mathbf{E}(t) - 2V\ \mathrm{Re}\{S(t)\nabla_0 S^*(t)\}, \tag{16b}$$

where

$$\nabla_0 S(t) \equiv i2^{3/2}V \int_{-\infty}^{t} dt'\ S(t')\ \frac{\mathbf{r}_0 + (i - t + t')\mathbf{v}_0}{[2 + i(t - t')]^{5/2}} \times \exp[i\mathscr{S}_0(t,t') + \Lambda(t,t')], \tag{16c}$$

using definitions for $\mathscr{S}_0(t,t')$ and $\Lambda(t,t')$ given in Eqs. (8c) and (10) respectively. After $S(t)$ has been found via Eq. (10), Eqs. (16) can be integrated in time to compute $\mathbf{d}(t)$. It is worth noting that Eqs. (16) depend only on time, having performed the spatial integration analytically over all space. Calculating the dipole moment in this way prevents any error introduced by considering a finite simulation domain, and is computationally more efficient than representing the wave function on a grid or with basis modes and computing $\mathbf{d}(t)$ directly with Eq. (14).

C. Bound probability and ionization rate

A time-dependent measure of the bound probability is given by the projection of $\psi(\mathbf{r},t)$ onto the electron's bound-state wave function, $\psi_0(\mathbf{r})$:

$$\rho_0(t) = |\langle \psi_0(\mathbf{r})|\psi(\mathbf{r},t)\rangle|^2. \tag{17}$$

The bound probability is related to the ionization rate w through the equation

$$\rho_0(t) = \rho_0(t_0)\exp\left[-\int_{t_0}^{t} dt'\ w(t')\right], \tag{18}$$

or

$$w(t) \equiv -\frac{d}{dt}\ln[\rho_0(t)/\rho_0(t_0)]\,. \tag{19}$$

While this is the most natural expression for the bound probability, it is not always the easiest to calculate. For this reason, we introduce two additional definitions for the electron bound probability. A particularly convenient measure of the bound probability for the NLI model is defined by projecting onto $u(\mathbf{r})$ in place of $\psi_0(\mathbf{r})$ and normalizing to unity:

$$\rho_u(t) \equiv \frac{|\langle u(\mathbf{r})|\psi(\mathbf{r},t)\rangle|^2}{|\langle u(\mathbf{r})|\psi(\mathbf{r},t=0)\rangle|^2} = \frac{|S(t)|^2}{|S(0)|^2}, \tag{20}$$

with associated ionization rate

$$w_u(t) \equiv -\frac{d}{dt}\ln\left[\rho_u(t)\right] = -\frac{d}{dt}\ln\left[\frac{|S(t)|^2}{|S(0)|^2}\right]. \tag{21}$$

The values of $\rho_0(t)$ and $\rho_u(t)$ [and hence $w(t)$, $w_u(t)$] are exactly equal when the electron is entirely bound, i.e., before the laser field is introduced. As the atom undergoes ionization, some fraction of the bound-electron wave function will transition to the continuum of free states, during which the projection of $\psi(\mathbf{r},t)$ onto $u(\mathbf{r})$ and $\psi_0(\mathbf{r})$ will not in general give the same result. After the pulse has passed, free components of the wave function continue to spread out in space, leaving only the remaining bound wave function to project significantly onto $u(\mathbf{r})$; free state contributions to $\rho_u(t)$ are accordingly reduced, and $\rho_u(t) \to \rho_0(t)$ in the long-time limit.

The extent that $\rho_u(t) \approx \rho_0(t)$ for intermediate times (i.e., during the simulation) depends on the similarity of the spatial profiles of $u(\mathbf{r})$ and $\psi_0(\mathbf{r})$. For parameters used to model atomic hydrogen, the spatial profiles of $u(\mathbf{r})$ and $\psi_0(\mathbf{r})$ are compared in Fig. 1(b). The similarity in profiles suggests that $\rho_u(t)$ should be a good approximation of $\rho_0(t)$—this is later confirmed with simulation results in Sec. V A. Moreover, the accuracy of $\rho_u(t)$ improves for larger values of the bound-state energy; if E_0 is increased (achieved by increasing V), the bound wave function $\psi_0(\mathbf{r})$ more closely conforms to $u(\mathbf{r})$, and $|S_0|^2 = |\langle u(\mathbf{r})|\psi_0(\mathbf{r})\rangle|^2$ approaches unity, as seen in Fig. 1(c). In the limit $E_0 \to \infty$, $\rho_u(t) = \rho_0(t)$ exactly. For the profile shown in Fig. 1(b), $|\langle u(\mathbf{r})|\psi_0(\mathbf{r})\rangle|^2 \approx 0.98$.

The last measure of bound probability considered in this paper does not directly relate the NLI model but is included here for organizational purposes and used exclusively in the *ab initio* simulation. Here, an approximate measure of the bound probability is given by the cumulative probability density of the electron wave function integrated out to radius $|\mathbf{r}| = \mathrm{r_c}$ and

normalized to unity at $t = 0$:

$$\rho_c(t) \equiv \frac{\int_{|\mathbf{r}|<r_c} d^3\mathbf{r}\ |\psi(\mathbf{r},t)|^2}{\int_{|\mathbf{r}|<r_c} d^3\mathbf{r}\ |\psi(\mathbf{r},0)|^2}. \tag{22}$$

This definition is convenient if the value of $\psi(\mathbf{r},t)$ is known, but requires a value of r_c to be chosen. Ideally, the value r_c is large enough to include the bound-electron wave function and small enough to exclude free wave-function components as they propagate outward; as these cannot be simultaneously satisfied (bound wave functions are generally infinite in spatial extent, and low momenta free states propagate slowly), there is some flexibility in the choice of r_c and hence the value of $\rho_c(t)$. As with the quantity $\rho_u(t)$, normalizing to the initial integrated probability ensures that $\rho_c(t)$ will match $\rho_0(t)$ at $t = 0$ and in the long-time limit.

Each of these definitions are included in this paper for separate reasons: While $\rho_0(t)$ is the most desirable measure of bound probability, it requires spatial integration of the wave function and is generally time consuming. By contrast, $\rho_u(t)$ is an approximate measure of bound probability, but efficiently obtained for the NLI model. Finally, the available data for the *ab initio* simulation is $\rho_c(t)$, and is used to calibrate the NLI model for suitable choice of r_c.

V. MODELING HYDROGEN

Having presented some of the basic properties of the NLI model, we now attempt to simulate atomic hydrogen. In particular, we would like to replicate the dipole response and ionization properties of atomic hydrogen for typical laboratory ultrashort laser pulse parameters.

We proceed by comparing simulations of the NLI model against two established models: an *ab initio* TDSE simulation, and a modified version of the well-known Keldysh ionization model [12]. Comparison to each of these provides a different type of validation. The *ab initio* simulation [23] numerically simulates the electron wave function time evolution via Eq. (3), and provides the highest fidelity treatment of the system we consider in this paper. While such a comparison is invaluable, the computational demands of full TDSE simulations allow a limited number of runs for comparison. To investigate the accuracy of the NLI over a range of different parameters, we turn to the Popruzhenko, Mur, Popov, and Bauer (PMPB) [25] ionization rate model. In contrast to the TDSE simulation, the PMPB model does not simulate the time dynamics of the electron wave function. Rather, it only predicts the atomic ionization rate for a monochromatic electric field. While the PMPB model offers significantly less information than a full TDSE simulation, it can be used to validate the NLI model over a large range of laser frequencies and intensities in relatively short computation time.

To compare the NLI model with those mentioned above, values must be determined for V and σ. The value for V was determined by Eq. (12) such that $E_0 = -13.6$ eV; in as far as we wish to simulate hydrogen, this is the only choice. This was modified slightly in the case of the *ab initio* simulation to match the numerical ground-state eigenenergy. The value of σ was determined by matching the total drop in bound probability of the NLI model with that of the *ab initio* simulation (Fig. 3), and used for all comparisons in this paper.

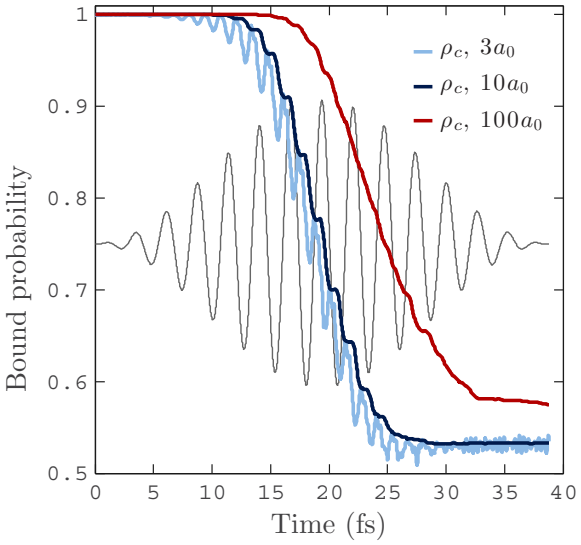

FIG. 2. (Color online) Measures of the bound probability given by Eq. (22) for three different radii in the *ab initio* simulation.

A. *ab initio* TDSE simulation comparison

A brief summary of the *ab intio* TDSE simulation is as follows: the Coulomb potential in Eq. (3) is replaced with a soft-core potential, $|\mathbf{r}|^{-1} \to (|\mathbf{r}|^2 + \delta\mathbf{r}^2)^{-1/2}$, where $\delta\mathbf{r} = 0.05$ a.u. is a small constant to accommodate the divergent Coulomb potential on a finite spatial grid. The Schrödinger equation is put into conservative form and $\psi(\mathbf{r},t)$ is propagated via the finite-volume method. The spatial domain consists of $4096 \times 32\,768$ $(r_\perp \times z)$ cells of size 0.04×0.04 a.u., and the time domain consists of $40\,000 \times 0.04$ a.u. time steps (approximately 40 fs). Use of the soft-core potential and finite spatial resolution results in a similar eigenspectrum as hydrogen for the first several bound states. The numerical ground-state energy is equal to $E_0 = -13.385$ eV.

In the simulation, a single hydrogen atom initially in the ground state is subjected to a 14.1 fs (full width at half maximum) linearly polarized laser pulse of 800 nm light with a maximum intensity $I_{\max} = 2.12 \times 10^{14}$ W/cm^2. The exact form of the field is $E(t) \equiv -\partial A_L/\partial t$ with $A_L(t) = A_0 \sin^2(\pi t/\tau)\cos(\omega_L t)$, where $A_0 = 1.37$, $\omega_L = 0.057$, and $\tau = 800$ in atomic units.

For the *ab initio* simulation, $\rho_c(t)$ was calculated for $r_c = 3, 10$, and 100 a.u., corresponding to initial integrated probabilities [numerator of Eq. (22)] of 0.934, 0.999 999 4, and $\sim$1, respectively. The results are plotted in Fig. 2 [with $\mathbf{E}(t)$ for reference], with some notable differences: The $r_c = 100a_0$ curve is still decreasing at 40 fs, indicating that free components of the wave function are still propagating out of the integration region, and therefore not a good measure of bound probability. To a lesser extent, this same effect smoothes out the features in the $r_c = 10a_0$ curve; the $3a_0$ curve is therefore the most appropriate of the three to use for comparison with the NLI model. The oscillatory features seen in the $3a_0$ curve are a result of the electric field distorting the (total) potential; as the applied field translates the minimum of the potential well, the "bound" portion of the wave function shifts against the fixed integration region, resulting in the

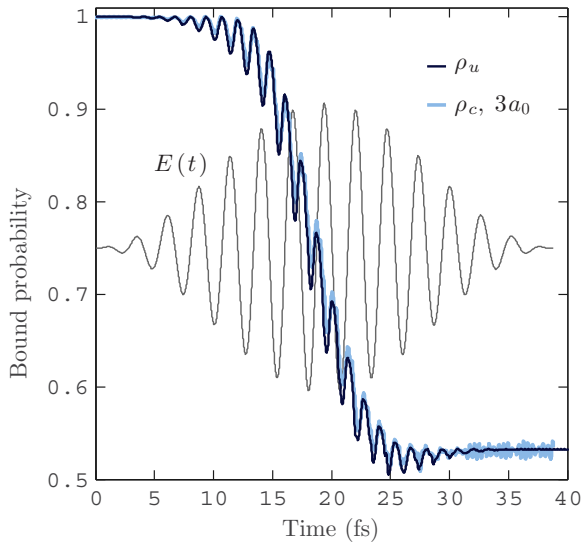

FIG. 3. (Color online) A comparison of the $r_c = 3a_0$ integrated probability (*ab initio* simulation) with the approximate bound probability $\rho_u(t)$ (NLI model).

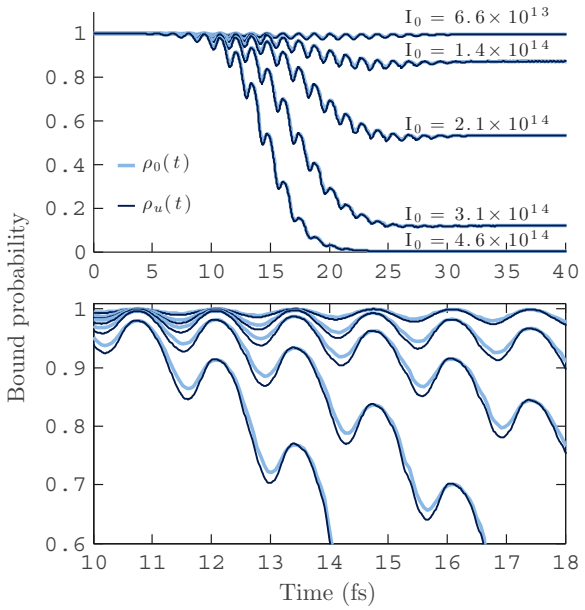

FIG. 4. (Color online) Top: a direct comparison of $\rho_u(t)$ (dark blue) with $\rho_0(t)$ (light blue) for the NLI model for five different laser intensities of a 14.1-fs 800-nm light laser pulse. The quantity $\rho_0(t)$ is produced by calculating $\psi_0(\mathbf{r})$ and $\psi(\mathbf{r},t)$ via Eqs. (13) and (9), respectively. These are then numerically integrated on a spatial grid $r_\perp \times z$ ($30a_0 \times 30a_0$) and normalized to the numerical value of $|\langle\psi_0(\mathbf{r})|\psi_0(\mathbf{r},t=0)|^2 = 0.95$. Bottom: an inset of the data is shown for greater detail. On the completion of each laser cycle (relative maxima), the plots agree to within 0.06%, the order of error in the normalization of $|\langle\psi_0(\mathbf{r})|\psi(\mathbf{r},t)\rangle|^2$.

observed minima. While this detail is largely absent in the $r_c = 10a_0$ curve, both curves give approximately the same bound probability by the end of the simulation, indicating that approximately 47% of the wave function has transitioned to free states and dispersed beyond $r_c = 10a_0$.

These data provide one means of calibrating the NLI model. On performing the analogous NLI simulation, the free parameter σ is adjusted such that the value of $\rho_u(t_f)$ matches that of $\rho_c(t_f)$ for the *ab initio* run. The value $\sigma = 2.494a_0$ was determined as a best fit for the $r_c = 3a_0$ *ab initio* run, shown in Fig. 3. Agreement of these curves demonstrates that the NLI model can produce an ionization rate similar to that obtained by the *ab initio* simulation as defined by Eq. (19) for these laser parameters. Later comparison with PMPB ionization theory demonstrates more generally that a single value of σ can be used to reproduce predicted ionization rates over a range of laser pulse intensities and frequencies.

Although this agreement suggests that $\rho_u(t)$ can be used as a measure of bound probability, it is worth examining how accurately $\rho_u(t)$ represents $\rho_0(t)$ as defined in Eq. (17) for the NLI model. Figure 4 compares $\rho_u(t)$ and $\rho_0(t)$ for several runs of various laser intensity. Values for $\psi_0(\mathbf{r})$ and $\psi(\mathbf{r},t)$ were calculated via Eqs. (9) and (13) on a spatial grid in $r_\perp \times z$ ($30a_0 \times 30a_0$), and numerically integrated to obtain $\rho_0(t)$. For the data provided, the accuracy of $\rho_0(t)$ is limited by integrating on a spatial grid and truncation of the integral in Eq. (9). This plot demonstrates the efficiency of the NLI model: $a \sim 1000\times$ increase in computation time required to compute $\rho_0(t)$ gives essentially the same result as given by $\rho_u(t)$.

Nevertheless, rendering $\psi(\mathbf{r},t)$ can be an aid to understanding the time dynamics of the system. Figure 5 shows a time series of the NLI electron wave function responding to $\mathbf{E}(t)$ (Fig. 3). Here, the probability density $|\psi(\mathbf{r},t)|^2$ is calculated in the $r_\perp \times z$ ($167a_0 \times 167a_0$) plane and plotted on a natural log scale. The first pane (0 fs) shows the bound-state probability density profile, the following six frames show the evolution over approximately one laser cycle from 10.5 to

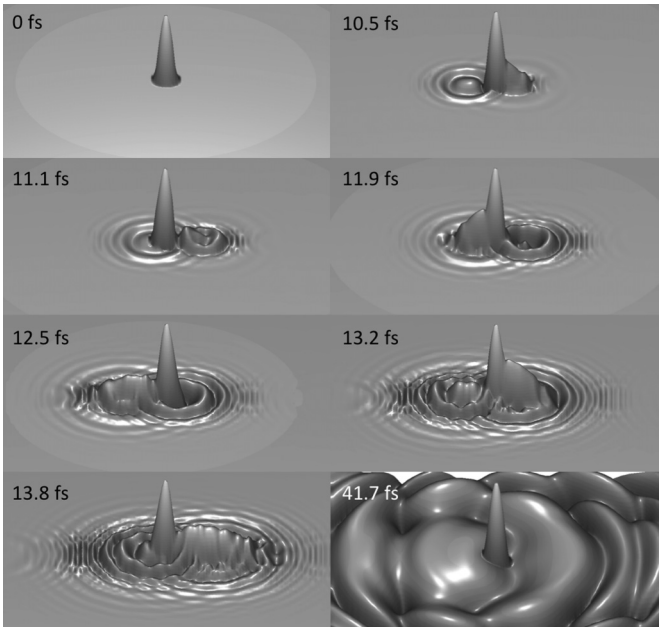

FIG. 5. The NLI wave function density in the $r_\perp \times z$ plane ($167a_0 \times 167a_0$), plotted on a natural log scale. The frames depict the bound-state profile (0 fs), approximately one laser cycle of evolution (10.5–13.8 fs), and a frame shortly after the laser pulse has passed (41.7 fs). Throughout, rescattering is observed as free components of the electron make subsequent passes across the binding potential.

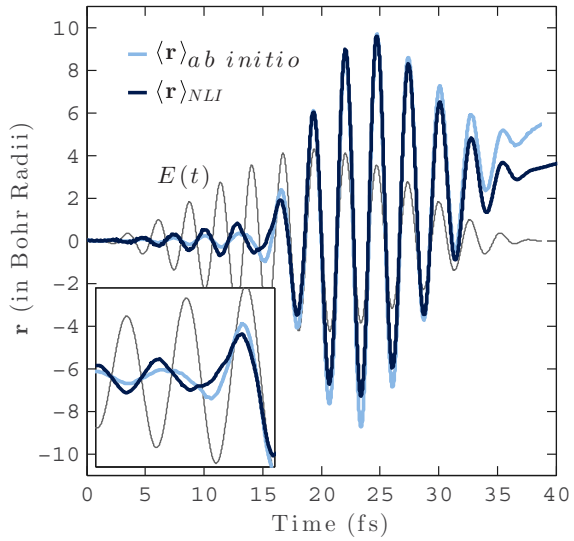

FIG. 6. (Color online) The predicted *ab initio* hydrogen and NLI dipole moments are compared. The inset (10–18 fs) shows the point at which the dipole transitions from a "bound" to "free" response. The dipole shown in the first half of the inset corresponds to the wave function depicted in Fig. 5.

13.8 fs, and the last frame shows the wave function shortly after the pulse has passed. The free components still in view at 41.7 fs do not contribute significantly to the bound probability (see Fig. 3) and continue to disperse from the region as time progresses. For these simulation parameters, the ionized wave function continues to interact with the binding potential over the course of the laser period, and interference patterns in the free wave function are observed. Such effects are accounted for in the NLI quantities $\rho_u(t)$ and $\langle \mathbf{r}(t) \rangle$, and are not included in ionization rate models. For this simulation, $\rho_u(t)$ and $\langle \mathbf{r}(t) \rangle$ can be calculated in less than a minute on a typical laptop computer.

The last quantity compared with the *ab initio* simulation is the dipole moment, $\mathbf{d}(t)$ $(-\langle \mathbf{r}(t) \rangle)$, shown in Fig. 6. Again, agreement is observed. One feature of interest occurs at approximately 13 fs, shown in the inset, at which point $\mathbf{r}(t)$ changes relative phase with the applied field $\mathbf{E}(t)$. Prior to 13 fs, both plots of $\langle \mathbf{r}(t) \rangle$ are seen to be out of phase with the electric field, and afterwards largely in phase. This can be understood in the following way: The "bound" electron response is largely out of phase with the field and initially dominates. As $\mathbf{E}(t)$ increases in strength, some of the electron wave function is excited to continuum states, leaving the vicinity of the ion and contributing as a "free" response to the dipole moment. Because the spatial excursions of the free wave function are large compared to the wave function in the ground state, a comparatively small fraction of unbound wave function will dominate the atomic dipole, causing the net dipole moment to change sign with respect to the field.

B. PMPB ionization theory comparison

In this section we compare the ionization rate predicted by the PMPB model with that of the NLI model as given by Eq. (21). The PMPB ionization model predicts the probability of ionization of a Coulomb bound electron in the presence of a low-field amplitude $[\max|\mathbf{E}(t)| < |E_0|/a_0]$ sinusoidally varying electric field. The rate shares the same exponential dependence on the electric-field amplitude as the rate predicted by Keldysh, but includes an improved field-dependent Coulomb correction. Direct comparison with the PMPB model is complicated by the fact that it only predicts a cycle averaged rate for monochromatic fields. Since NLI simulations are performed in the time domain and require that $E(t) = 0$ on the semi-infinite range of $t < t_0$, any electric field is necessarily enveloped and therefore contains a range of intensities and frequency components.

For this reason, it is easier to perform laser pulse simulations in the time domain and compare the net ionization predicted by the NLI and PMPB models. We define an effective ionization rate in terms of the total drop in bound probability and full width half maximum pulse time as

$$w_{\text{eff}} \equiv -\frac{1}{T_{\text{fwhm}}} \ln[\rho(t_f)/\rho(t_0)]. \tag{23}$$

To compute w_{eff} for the PMPB model, the PMPB rate is first converted to a bound probability based via Eq. (17) based on the field envelope, which is then evaluated after the the pulse has passed to generate w_{eff}. To analogous quantity for the NLI model is given by calculating $\rho_u(t)$ [Eq. (20)], and again evaluating after the pulse has passed. For all the NLI data compared with the PMPB rate model, a best-fit value is used of $\sigma = 2.45a_0$ (2% different than the value used to match the *ab initio* simulation), and V was chosen via Eq. (12) such that $|E_0| = 13.6$ eV for both the PMPB and NLI models.

1. Frequency dependence

Comparison of the frequency dependence is a crucial test for the NLI model. The PMPB model predicts a strong dependence of ionization rate on the laser frequency, with local maxima in the rate w occurring for each N-photon resonance, when $N\hbar\omega_{\text{laser}} \approx |E_0|$. This expression is only approximate because the laser field distorts the effective binding potential energy (i.e., they are ac stark shifted [26]). To compare the frequency dependence of the PMPB and NLI ionization rates, simulations were performed in which a hydrogen atom is subject to a single frequency laser pulse, and w_{eff} computed for both models. The electric-field envelope is piecewise defined to have a 15-fs $\sin^2(t)$ ramp to a constant amplitude of 1×10^{13} W/cm^2 for 55 fs before symmetrically ramping back down to zero; this profile was chosen to minimize dependence of the ionization rate on intensity and isolate frequency dependence in w_{eff}. Figure 7 shows the results for several simulations of varied carrier frequency. The NLI model is seen to reproduce each N-photon resonance predicted by the PMPB model; the highest peak occurs at the single-photon ionization rate, where $\hbar\omega_{\text{laser}} \approx 1.2|E_0|$. Above this frequency, the ionization rate drops off as the electron cannot respond quickly enough to the laser field oscillations. On increasing the intensity of the laser to 1.9×10^{13} W/cm^2, the procedure was repeated for typical laboratory laser frequencies, shown in the bottom panel of Fig. 7.

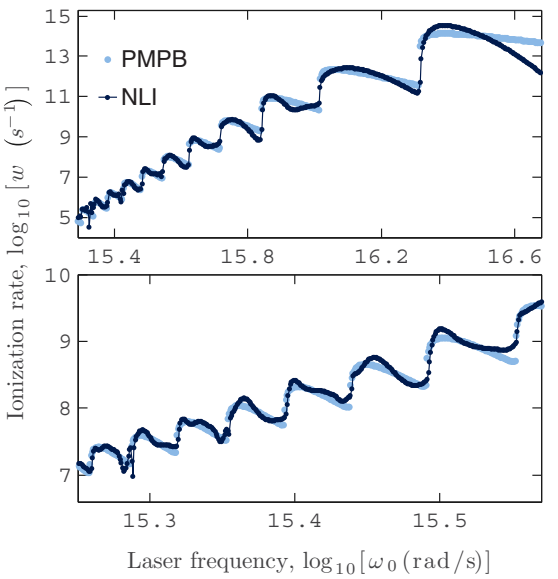

FIG. 7. (Color online) Top: the PMPB and NLI effective ionization rates (w_{eff}) show agreement when compared over a range of frequencies. Bottom: the same result for optical frequencies, with the laser intensity increased to $I_0 = 1.9 \times 10^{13}$ W/cm^2.

2. Intensity dependence

The intensity dependence of the NLI and PMPB models was also compared. Here, a hydrogen atom is subject to an 14.6-fs 800 nm laser pulse with a $\sin^2(t)$ envelope, and w_{eff} calculated for both models. This procedure was repeated while varying peak laser intensity and plotted in Fig. 8. The lower limit of ionization rate detection is limited by the accuracy of measuring changes in $\rho_u(t)$, while agreement at high intensity is limited by the effect of depletion: at 1×10^{15} W/cm^2, the electron is (almost) completely ionized before the end of the pulse. Residual

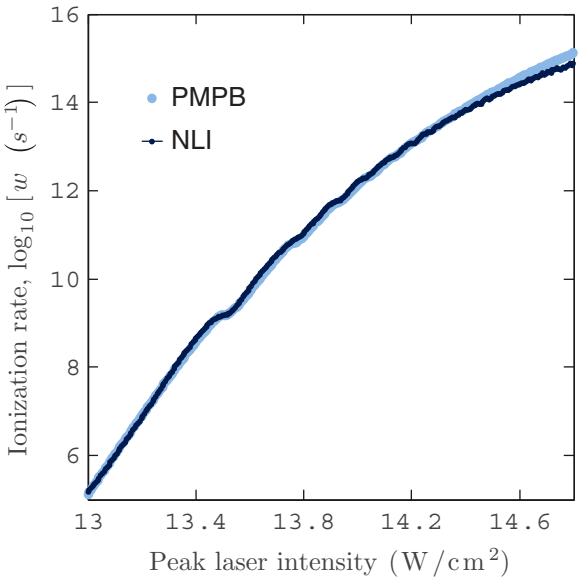

FIG. 8. (Color online) Intensity dependence of the NLI and PMPB effective ionization rate for a 14.6-fs pulse of 800-nm light.

wave function in the vicinity of $u(\mathbf{r})$, either from rescattering events or numeric in origin, eventually suppresses the NLI effective rate when compared with the PMPB effective rate.

VI. EXTENSIONS OF THE NLI MODEL

One of the noticeable omissions of the NLI model, as explored in this paper, is the existence of multiple bound states. While the single state model is appropriate for many systems in the single active electron regime, there is utility in including multiple bound states; it has been suggested, for example, that the presence of additional bound states can have an effect on the nonlinear polarizability of atoms [27]. The NLI model explored in this paper can be extended to include an arbitrary number of bound states using the following substitution:

$$V u(\mathbf{r}) S(t) \to \sum_i^N V_i u_i(\mathbf{r}) S_i(t), \tag{24a}$$

$$S_i(t) \to \int d^3\mathbf{r}\, u_i(\mathbf{r}) \psi(\mathbf{r},t), \tag{24b}$$

where $u_i(\mathbf{r})$ represents a set of orthogonal basis functions. The NLI model then permits N bound states with eigenvalues determined by the associated V_i. A natural choice of basis functions is the three-dimensional Gaussian-Hermite polynomials of which the $u(\mathbf{r})$ used in this paper is the first, but other choices are possible. Multiple bound states will be explored in future work.

VII. CONCLUSIONS

This paper examines a phenomenological nonlocal potential model for the atomic response to a laser electric field. When compared to an *ab initio* simulation of atomic hydrogen, the NLI model gives remarkably accurate results for the bound probability and atomic dipole moment. Further comparisons show agreement with the PMPB model and NLI model predicted ionization rates over a range of laser frequencies and intensities. The ability to obtain these results for a 3D quantum simulation with extremely low computational overhead (when compared to *ab initio* TDSE simulations) makes the NLI model a promising tool for investigating laser ionization and propagation phenomena.

ACKNOWLEDGMENTS

The authors would like to acknowledge L. Johnson for fruitful discussions. This work was supported by funding from ONR and DOE.

APPENDIX

Here we provide a sketch of the method used to treat the infinite integral in Eq. (10). We begin by representing the integral equation for $S(t)$ schematically as

$$S(t) = \int_{-\infty}^{t} dt' K(t,t') S(t'), \tag{A1}$$

where $\mathbf{E}(t) = 0$ for $t < 0$. We would like to make use of the fact that the integral contribution over the infinite past can be

expressed analytically in the absence of $E(t)$:

$$S(t) = \int_{-\infty}^{0} dt' K_0(t,t') S(t') = \frac{2^{5/2} V}{\sqrt{2+it}} [1 - \sqrt{(2+it)\pi |E_0|} \times \mathrm{erfc}(\sqrt{(2+it)|E_0|}) e^{(2+it)|E_0|}], \quad \text{(A2)}$$

where $K_0(t,t')$ is the field free kernel in Eq. (11). We rewrite the general form of $S(t)$ by splitting the integral as follows:

$$S(t) = \int_{-\infty}^{0} dt' K_1(t,t') S(t') + \int_{0}^{t} dt' K(t,t') S(t'), \quad \text{(A3)}$$

where

$$K_1(t,t') = \frac{2^{3/2} i V}{[2+i(t-t')]^{3/2}} \exp\left[i\mathscr{S}(t;0) - \frac{1}{2}\mathbf{r}_0^2(t;0) \right] \exp\left[\frac{1+i(t-t')}{2+i(t-t')} \frac{|\mathbf{r}_0(t;0) - i\mathbf{v}_0(t;0)|^2}{2} \right]. \quad \text{(A4)}$$

The trajectory variables $\mathbf{v}_0(t;0)$, $\mathbf{r}_0(t;0)$ in K_1 depend only on t, inviting the kernel to be written in terms of $K_0(t,t')$ as follows:

$$K_1(t,t') = f(t) K_0(t,t') - f(t) K_0(t,t') \left[1 - \exp\left(\frac{-|\mathbf{r}_0(t;0) - i\mathbf{v}_0(t;0)|^2}{4 + 2i(t-t')} \right) \right], \quad \text{(A5)}$$

where

$$f(t) \equiv \exp\left[i\mathscr{S}(t;0) - \frac{1}{2}\mathbf{r}_0^2(t;0) + \frac{|\mathbf{r}_0(t;0) - i\mathbf{v}_0(t;0)|^2}{2} \right]. \quad \text{(A6)}$$

The advantage gained is that the first term in Eq. (A5) is solvable analytically via Eq. (A2), since $f(t)$ can be pulled out of the integral over t'. Although the remaining terms (in square brackets) must be truncated and solved numerically, they vanish in the limit that $E(t) \to 0$ (i.e., $\mathbf{v}_0, \mathbf{r}_0 \to 0$) and as $(t - t') \gg 1$. Evaluating $S(t)$ this way permits a smooth transition from the analytic value of $S(t < 0)$ to the numerically calculated value for $S(t > 0)$, whereas truncation of the integral in Eq. (A1) creates a sharp discontinuity even for $E(t) = 0$. Finally, calculating the second term in Eq. (A3) is straightforward, having obtained the history of $S(t)$ by the method outlined above.

[1] V. Malka, *Proceedings of the Fourth International Particle Accelerator Conference (IPAC2013)* (JACoW, http://accelconf.web.cern.ch/AccelConf/IPAC2013/papers/moybb101.pdf, 2013), pp. 11–15.
[2] L. Johnson and J. Palastro, Phys. Rev. A **88**, 063804 (2013).
[3] K.-Y. Kim, J. H. Glownia, A. J. Taylor, and G. Rodriguez, Opt. Express **15**, 4577 (2007).
[4] J. L. Krause, K. J. Schafer, and K. C. Kulander, Phys. Rev. Lett. **68**, 3535 (1992).
[5] A. Couairon and A. Mysyrowicz, Phys. Rep. **441**, 47 (2007).
[6] Y.-H. Chen, S. Varma, T. M. Antonsen, and H. M. Milchberg, Phys. Rev. Lett. **105**, 215005 (2010).
[7] J. K. Wahlstrand, Y.-H. Cheng, Y.-H. Chen, and H. M. Milchberg, Phys. Rev. Lett. **107**, 103901 (2011).
[8] J. P. Palastro, T. M. Antonsen, and H. M. Milchberg, Phys. Rev. A **86**, 033834 (2012).
[9] A. Couairon, E. Brambilla, T. Corti, D. Majus, O. Ramírez-Góngora, and M. Kolesik, Eur. Phys. J. Spec. Top. **199**, 5 (2011).
[10] M. Kolesik and J. V. Moloney, Rep. Prog. Phys. **77**, 016401 (2014).
[11] P. Sprangle, J. R. Peñano, and B. Hafizi, Phys. Rev. E **66**, 046418 (2002).
[12] L. V. Keldysh, Zh. Eksp. Teor. Fiz. **47**, 1515 (1964) [Sov. Phys. JETP **20**, 1307 (1965)].
[13] A. M. Perelomov, V. S. Popov, and M. V. Terent'ev, JETP **23**, 924 (1966).
[14] N. B. Delone and V. P. Krainov, Phys. Usp. **41**, 469 (1998).
[15] D. Bauer and P. Mulser, Phys. Rev. A **59**, 569 (1999).
[16] G. L. Yudin and M. Y. Ivanov, Phys. Rev. A **64**, 013409 (2001).
[17] V. S. Popov, J. Phys. Usp. **47**, 855 (2004).
[18] T. Walsh and F. Ilkov, J. Phys. B **27**, 3767 (1994).
[19] A. Talebpour, J. Yang, and S. Chin, Opt. Commun. **163**, 29 (1999).
[20] H. M. Tetchou Nganso, Y. V. Popov, B. Piraux, J. Madroñero, and M. G. K. Njock, Phys. Rev. A **83**, 013401 (2011).
[21] A. Teleki, E. M. Wright, and M. Kolesik, Phys. Rev. A **82**, 065801 (2010).
[22] H. Kono, A. Kita, Y. Ohtsuki, and Y. Fujimura, J. Comput. Phys. **130**, 148 (1997).
[23] D. Gordon and B. Hafizi, J. Comput. Phys. **231**, 6349 (2012).
[24] D. Bauer and P. Koval, Comput. Phys. Commun. **174**, 396 (2006).
[25] S. V. Popruzhenko, V. D. Mur, V. S. Popov, and D. Bauer, Phys. Rev. Lett. **101**, 193003 (2008).
[26] N. Delone and V. Krainov, Phys. Usp. **42**, 669 (1999).
[27] J. Andreasen, E. M. Wright, and M. Kolesik, IEEE J. Quantum Electron. **49**, 1088 (2013).